68

Research Article

JUCVM Journal of Updates in Cardiovascular Medicine

J Updates Cardiovasc Med 2026;14(3):68-78 **DOI:** 10.32596/jucvm.galenos.2025.2026-7-184

Metal Artifact Reduction in Chest CT of Patients with Cardiac Implantable Devices

Özgür Genç[1], Serap Baş[2], Ömer Naci Tabakçı[3]

[1]İstanbul Aydın University Faculty of Medicine, Department of Radiology, İstanbul, Türkiye
[2]University of Health Sciences Türkiye, Başakşehir Çam and Sakura City Hospital, Clinic of Radiology, İstanbul, Türkiye
[3]University of Health Sciences Türkiye, KocaeliCity Hospital, Clinic of Radiology, Kocaeli, Türkiye

Abstract

Objectives: To determine whether smart metal artifact reduction (SMAR) combined with adaptive statistical iterative reconstruction (ASIR) improves thoracic computed tomography (CT) image quality in patients with cardiac implantable electronic devices (CIEDs) compared with ASIR alone.

Materials and Methods: In this retrospective single-center study (January 2022-December 2024), 30 consecutive CIED carriers (mean age 63.4±14.5 years; 18 pacemakers, 12 implantable cardioverter-defibrillators) who underwent thoracic CT on a 512-slice scanner were evaluated. Paired ASIR-only and ASIR+SMAR reconstructions were generated from identical raw data. Two blinded radiologists graded image quality on a 5-point scale across soft-tissue, osseous, and pulmonary windows at proximal (<3 cm), intermediate (3-5 cm), and distal (>5 cm) zones. A third radiologist measured quantitative artifact load as the Hounsfield unit standard deviation (HU-SD) in proximal-zone regions of interest.

Results: ASIR+SMAR significantly reduced proximal-zone HU-SD compared with ASIR alone (43.60±17.33 vs. 90.40±42.11; $p<0.001$; Cohen's $d=1.42$), representing a 52% reduction. Overall qualitative scores improved significantly (3.84±0.48 vs. 2.92±0.47; $p<0.001$). The greatest gains occurred on the soft-tissue windows in the proximal and intermediate zones ($p<0.001$). However, algorithm-related streaks appeared in distal lung parenchyma in 13 of 30 patients (43.3%), with 5 (16.7%) being severe enough to preclude evaluation. Inter-reader agreement was substantial (weighted κ: 0.68-0.72).

Conclusion: SMAR combined with ASIR significantly improves image quality metrics in the proximal and intermediate zones around CIED generators. However, algorithm-induced artifacts in distal lung parenchyma occur in approximately 43% of patients. A dual-reconstruction review strategy is recommended for clinical practice.

Keywords: Thoracic computed tomography, metal artifact reduction, cardiac pacemaker, implantable cardioverter-defibrillator, iterative reconstruction

Address for Correspondence: Özgür Genç, İstanbul Aydın University Faculty of Medicine, Department of Radiology, İstanbul, Türkiye
e-mail: drozgurgenc@gmail.com **ORCID:** orcid.org/0009-0009-3901-223X
Received: 05.04.2026 **Accepted:** 25.06.2026 **Publication Date:** 25.09.2026

Cite this article as: Genç Ö, Baş S, Tabakçı ÖN. Metal artifact reduction in chest CT of patients with cardiac implantable devices. J Updates Cardiovasc Med. 2026;14(3):68-78

DOI: 10.32596/jucvm.galenos.2025.2026-7-184

Introduction

The clinical deployment of cardiac implantable electronic devices (CIEDs)—encompassing pacemakers, implantable cardioverter-defibrillators (ICDs), and cardiac resynchronization therapy systems—has expanded steadily as therapeutic indications broaden and populations age. These devices generally comprise a subcutaneous pulse generator positioned in the infraclavicular region together with one or more endovascular leads coursing through the central venous system to the myocardium[1]. Although magnetic resonance imaging capabilities have advanced, thoracic computed tomography (CT) retains a central role in chest assessment, offering high-resolution depiction of pulmonary, mediastinal, cardiac, and musculoskeletal anatomy. Nevertheless, the metallic housing of the pulse generator frequently gives rise to image degradation that hampers evaluation of neighboring structures and diminishes overall diagnostic utility[2].

The physical mechanisms underlying metallic artifacts primarily involve beam hardening, photon starvation, and X-ray scatter[3]. Multiple remediation strategies have been proposed. Fundamental acquisition-level approaches include increasing tube potential and current, narrowing collimation, using iterative reconstruction kernels, applying softer convolution filters, and increasing the reconstructed section width[2,4]. A distinct paradigm leverages dual-energy CT to generate virtual monoenergetic datasets at selected photon energies, thereby attenuating beam-hardening effects;[5-7] however, this benefit wanes with high-atomic-number alloys, bulky hardware, and angular geometries. A third category employs projection-domain metal artifact reduction (MAR) software that detects corrupted sinogram projections passing through metallic components and substitutes them with estimated values derived from adjacent, unaffected data[8,9].

Published evidence indicates that MAR processing can meaningfully diminish artifactual degradation in post-operative thoracic CT images and bolster image interpretability[10,11]. At the same time, MAR algorithms may occasionally engender secondary artifacts, particularly at locations remote from the implant, and vendor-specific implementations can produce divergent outcomes[9,12]. The most pertinent prior investigation involving CIEDs was reported by Pennig et al.[6] who examined virtual monoenergetic images and MAR post-processing derived from spectral-detector CT in a 34-patient cohort. That work confirmed artifact mitigation around both the generator and the leads, yet did not evaluate pulmonary parenchymal windows or delineate how MAR-induced artifacts vary with distance from the hardware.

Notwithstanding these contributions, rigorous assessment of proprietary MAR solutions across diverse tissue displays and at graduated distance intervals among CIED carriers remains sparse. In particular, the GE smart metal artifact reduction (SMAR) algorithm has not been evaluated in this patient population across soft-tissue, osseous, and pulmonary windows and across defined spatial strata, nor has any report systematically mapped the distance-dependent emergence of algorithm-related artifacts in the lung fields of CIED recipients.

Accordingly, the present investigation was designed to retrospectively appraise the influence of SMAR, applied in conjunction with adaptive statistical iterative reconstruction (ASIR), on thoracic CT image quality in CIED carriers, compared with ASIR alone, using both quantitative artifact metrics and qualitative reader-based evaluations across predetermined tissue displays and distance intervals.

Materials and Methods

This single-institution retrospective analysis adhered to the principles of the Declaration of Helsinki and was structured following the Strengthening the Reporting of Observational Studies in Epidemiology (STROBE) framework. Institutional Ethics Committee approval was obtained İstanbul Yeni Yüzyıl University Clinical Research Ethics Committee (decision no: 2021/04-653, date: 06/04/2021), and the requirement for informed consent was waived because of the retrospective nature of the study and the exclusive use of anonymized datasets.

Study Design and Participant Selection

We identified all consecutive CIED carriers who underwent thoracic CT at our facility between January 2022 and December 2024. Eligibility was determined according to the following criteria:

Inclusion criteria: (a) a functioning CIED (pacemaker, ICD, or cardiac resynchronization device) present during the CT acquisition, and (b) complete availability of both ASIR-only and ASIR+SMAR image datasets generated from the same scan.

Exclusion criteria: (a) incomplete or technically failed image reconstructions attributable to archival malfunction or algorithmic error, and (b) clinically meaningful pulmonary parenchymal abnormality—operationally defined as radiologically apparent consolidation, ground-glass attenuation spanning more than a single lobe, diffuse interstitial lung disease, substantial pleural effusion (occupying >1/3 of the hemithorax), or history of pulmonary resection. This restriction was imposed to maintain uniform baseline lung tissue characteristics, thereby ensuring reliable artifact quantification and consistent region-of-interest placement.

Of 35 consecutively identified patients, 5 were excluded owing to technically incomplete reconstructions: archiving errors disrupted ASIR datasets in 3 cases, while SMAR processing failed in the remaining 2 cases. The resultant analytic cohort numbered 30 individuals.

Sample Size Rationale

The sample size was determined by the number of consecutive eligible patients identified during the predefined study period. Given the retrospective design of the study, no formal a priori sample size calculation was performed. The final cohort consisted of 30 paired observations. Therefore, analyses of secondary endpoints should be interpreted with caution and considered exploratory.

Demographic and Device Data

Clinical demographics and device specifications were extracted from institutional electronic health records. Recorded variables included age, sex, body mass index (BMI), reason for CT referral, intravenous contrast use, device category (pacemaker, ICD, or cardiac resynchronization system), hardware manufacturer, lead count and configuration (single-chamber, dual-chamber, or biventricular), and generator laterality.

Image Acquisition Protocol and Reconstruction

Every examination was acquired on a single-source, 512-slice platform (Revolution CT, GE Healthcare, USA) using the following parameters: tube potential 120 kVp, tube current modulation via SmartmA (range 100–500 mA), detector aperture 40 mm, helical pitch factor 0.992, gantry rotation period 0.80 s, reconstructed section thickness 1.25 mm, section increment 1.25 mm, and display field of view 50 cm. Radiation exposure was tracked through DICOM-structured dose reports to facilitate ongoing optimization[13].

Two reconstruction pipelines were applied to identical raw projection datasets. ASIR, a hybrid iterative technique operating in both the projection and image domains, models photon and electronic noise statistics and iteratively refines the image by comparing forward-projected estimates with acquired data; the 50% blending ratio—our institutional default—was selected as the optimal trade-off between noise suppression and texture preservation. SMAR is a projection-completion algorithm that segments high-attenuation metal voxels by thresholding, identifies the corrupted “metal trace” within the sinogram, replaces those samples, guided by a prior image, with values interpolated from adjacent uncorrupted projections, and reconstructs the corrected sinogram with ASIR before reinserting the metal voxels. The manufacturer-defined “thorax” preset, employed throughout, incorporates chest-optimized segmentation thresholds and interpolation kernels. Both reconstructions used identical raw data, required no modification of the acquisition protocol, and added approximately 60–90 seconds of offline workstation processing time per dataset when using the SMAR pipeline[14,15].

Paired image sets were interpreted on an Advantage Windows Workstation 4.7 (GE Healthcare, Milwaukee, WI). Three display configurations were employed: soft-tissue [window width 400 Hounsfield unit (HU), center 35 HU], osseous (width 2500 HU, center 480 HU), and pulmonary (width 1500 HU, center −600 HU). Assessment was confined to the axial orientation.

Outcome Definitions

Two co-primary endpoints were designated: (1) quantitative artifact load, operationalized as the standard deviation of (HU-SD) within proximal zone regions of interest (ROI) adjacent to the pulse generator, and (2) aggregate qualitative image-quality score. Secondary endpoints comprised qualitative ratings for each of the nine display–zone pairings (soft-tissue, osseous, and pulmonary displays across proximal, intermediate, and distal zones), together with the frequency and severity classifications of algorithm-related artifacts arising in the distal lung parenchyma.

Qualitative Image Appraisal

Two independent readers with thoracic CT interpretation experience (Reader A: 16 years; Reader B: 10 years) conducted qualitative assessments under blinded conditions. ASIR and ASIR+SMAR datasets were displayed in randomized sequence during workstation sessions separated by a minimum 14-day interval. Neither reader was informed of the reconstruction method applied to a given image set.

Global image quality was graded on a 5-point ordinal scale: 1= severe degradation rendering adjacent anatomy invisible; 2= pronounced artifacts causing substantial distortion; 3= moderate artifacts permitting structural identification; 4= minor artifacts with slight blurring; 5= artifact-free appearance.

In addition, each of the three display settings (soft-tissue, osseous, and pulmonary) was evaluated at three graduated distance bands from the device: proximal (<3 cm), intermediate (3–5 cm), and distal (>5 cm), producing nine display–zone combinations.

Algorithm-induced artifacts were characterized separately on a 3-tier scale: 1= absent; 2= present but permitting diagnostic interpretation; 3= present and precluding diagnostic interpretation. Such artifacts were operationally defined as degradations present in the ASIR+SMAR dataset but absent from the corresponding ASIR-only images.

When readers' scores diverged, disagreements were adjudicated through structured discussion. In 4 of 270 aggregate display–zone evaluations (1.5%), consensus was unattainable; therefore, the arithmetic mean of the two ratings was adopted; these averaged values were rounded to the nearest whole number prior to statistical testing to preserve ordinal data integrity.

Quantitative Artifact Assessment

A third radiologist (Reader C, 12 years of thoracic CT experience, uninvolved in qualitative assessment) performed objective measurements by positioning three elliptical (ROIs, each with a fixed 1.5-cm diameter) within the proximal zone adjacent to the pulse generator on the axial section exhibiting peak artifact intensity. ROIs were systematically placed at three anatomically defined sites: (1) anteriorly, (2) medially, and (3) posteriorly relative to the device, deliberately avoiding overlap with major vasculature or aerated lung, in accordance with the measurement protocol of Subhas et al.[11]. The HU-SD within each ROI was recorded, and the arithmetic mean across all three ROIs constituted the quantitative artifact index. Elevated HU-SD values denote greater artifact contamination.

Measurement reproducibility was assessed in two ways. For inter-observer reliability, a fourth radiologist (Reader D, 8 years of experience) independently repeated the measurements on a randomly selected subset of 10 patients (33%), following the same protocol. To assess intra-observer consistency, Reader C remeasured the same 10-patient subset after a 3-week interval. Two-way mixed-model intraclass correlation coefficients (ICCs) with absolute agreement were computed for both reliability dimensions.

Mitigation of Potential Bias

Multiple safeguards were instituted to limit systematic error. Qualitative raters were blinded to the reconstruction strategy, and the display order was randomized. Quantitative measurements were conducted by an independent reader to prevent contamination by qualitative impressions. ROI placement adhered to a fixed-size, anatomically predetermined protocol. Consecutive enrollment minimized selection bias. Inter- and intra-observer reproducibility was formally quantified. Notwithstanding these precautions, unmeasured confounders and institutional workflow characteristics inherent in a retrospective single-site design cannot be fully excluded.

Statistical Analysis

Analyses were performed using SPSS version 28.0 (IBM Corp., Armonk, NY). Continuous variables are reported as mean ± standard deviation; medians and interquartile ranges are additionally provided when distributions depart from normality. The Shapiro-Wilk test was used to assess the distributional form of the data, and Levene's test was used to assess the homogeneity of variances.

Co-primary endpoints were compared using for data that were normally distributed, with results expressed as mean differences, 95% confidence interval (CI), and p-value. A two-sided significance threshold of $p<0.05$ was applied to the two co-primary comparisons. For the nine secondary display–zone contrasts, a Bonferroni-adjusted threshold of $p<0.0056$ ($0.05 \div 9$) was enforced. Paired data that were not normally distributed were analyzed using Wilcoxon signed-rank tests. Categorical frequencies were compared using Fisher's exact test. The particular test employed for each comparison is specified in the Results.

Paired effect sizes were quantified using Cohen's d. Inter-reader concordance for ordinal qualitative scores was evaluated using weighted kappa (linear weighting) with 95% CIs; interpretive benchmarks followed Landis and Koch: 0–0.20 slight, 0.21–0.40 fair, 0.41–0.60 moderate, 0.61–0.80 substantial, 0.81–1.00 nearly perfect. Linear-weighted kappa was preferred to its unweighted counterpart because ordinal scales penalize larger discrepancies more heavily.

To gauge robustness against the interval-scale assumption underlying parametric analysis of ordinal ratings, all primary and secondary paired comparisons initially analyzed by t-test were replicated using Wilcoxon signed-rank tests as a pre-specified sensitivity check.

Five individuals were excluded because of incomplete reconstructions; the remaining 30 had complete data for every measurement. No additional missing values existed among objective or qualitative endpoints, obviating the need for imputation procedures.

Results

Cohort Characteristics

Of the 35 screened individuals, 30 met all eligibility requirements and were included in the final analysis. Mean age was 63.4 ± 14.5 years (range 25-89), with a female-to-male ratio of 16:14 (53.3% vs. 46.7%). Mean BMI was 27.8±5.2 kg/m^2. The primary reasons for CT referral were surveillance (n=14, 46.7%), investigation of breathlessness (n=8, 26.7%), suspected infectious complications (n=5, 16.7%), and procedural planning (n=3, 10.0%). Intravenous contrast was administered in 22 studies (73.3%).

The cohort comprised two CIED categories: conventional pacemakers (18 patients, 60.0%) and transvenous ICDs (12 patients, 40.0%); no isolated CRTs, subcutaneous ICDs, or leadless devices were represented. Lead configurations were single-chamber (one right ventricular lead) in 8 patients (26.7%), dual-chamber (right atrial plus right ventricular leads) in 16 (53.3%), and biventricular (right atrial, right ventricular, and coronary sinus leads) in 6 (20.0%), yielding 60 endovascular leads in total (mean 2.0 per patient). Hardware devices were manufactured by Medtronic (n=14, 46.7%); Boston

Scientific (n=9, 30.0%); Abbott/St. Jude (n=5, 16.7%); and Biotronik (n=2, 6.7%). Generators were positioned in the left infraclavicular pocket in 27 patients (90.0%) and in the right infraclavicular pocket in 3 patients (10.0%). Full demographic and device data appear in Table 1.

Distribution Testing

The Shapiro-Wilk test confirmed that HU-SD values were normally distributed for both the ASIR series (W=0.961, p=0.327) and the ASIR+SMAR series (W=0.953, p=0.208), supporting the use of the paired t-test. Global qualitative scores likewise conformed to normality across both reconstruction methods (all p>0.05).

Descriptive Visual Observations

On soft-tissue displays, ASIR+SMAR reproducibly attenuated proximal-zone streaking and beam-hardening artifacts, enhancing the depiction of peri-device musculature and vascular anatomy relative to ASIR alone (Figure 1). In the intermediate zone (Figure 2), osseous structures showed diminished metallic degradation and sharper cortical delineation of thoracic skeletal elements. Pulmonary images demonstrated reduced proximal-zone artifacts with ASIR+SMAR; however, distal-zone (>5 cm) band-like streaks were intermittently noted in aerated parenchyma (Figure 3).

Table 1. Demographic and device profile of the study cohort (n=30)

Variable	Result
Age, years (mean ± SD)	63.4±14.5
Age range, years	25–89
Female sex, n (%)	16 (53.3)
BMI, kg/m² (mean ± SD)	27.8±5.2
Contrast-enhanced study, n (%)	22 (73.3)
Referral indication, n (%)	
Surveillance	14 (46.7)
Breathlessness workup	8 (26.7)
Suspected infection	5 (16.7)
Procedural planning	3 (10.0)
Device category, n (%)	
Pacemaker	18 (60.0)
ICD	12 (40.0)
Hardware manufacturer, n (%)	
Medtronic	14 (46.7)
Boston scientific	9 (30.0)
Abbott/St. Jude	5 (16.7)
Biotronik	2 (6.7)
Lead arrangement, n (%)	
Single-chamber	8 (26.7)
Dual-chamber	16 (53.3)
Biventricular	6 (20.0)
Left-sided generator, n (%)	27 (90.0)

SD: Standard deviation, BMI: Body mass index, ICD: Implantable cardioverter-defibrillator

Quantitative Artifact Load (Co-primary Endpoint 1)

Mean HU-SD in proximal-zone ROIs (<3 cm from the generator) was substantially lower with ASIR+SMAR than ASIR alone (43.60±17.33 vs. 90.40±42.11), corresponding to a 52% decrement. The mean paired

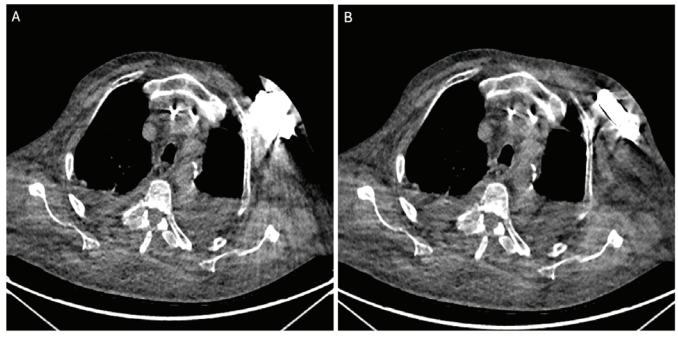

Figure 1. Soft-tissue window in a CIED patient: ASIR+SMAR reduces peri-device streak and beam-hardening and improves depiction of adjacent soft tissues and vascular structures compared with ASIR
CIED: Cardiac implantable electronic device, ASIR: Adaptive statistical iterative reconstruction, SMAR: Smart metal artifact reduction

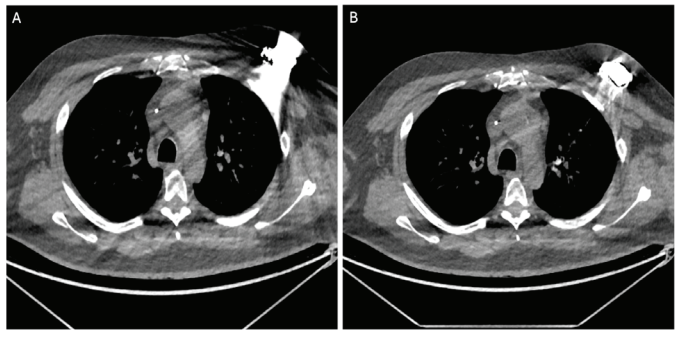

Figure 2. On bone-window images, ASIR+SMAR reduces metallic artifacts and improves visualization of the cortical bone and thoracic skeleton adjacent to the generator compared with ASIR
ASIR: Adaptive statistical iterative reconstruction, SMAR: Smart metal artifact reduction

difference was 46.80 HU (95% CI: 38.2–55.4; paired t-test, p<0.001; Cohen's d=1.42). This comparison is graphically summarized in Figure 4.

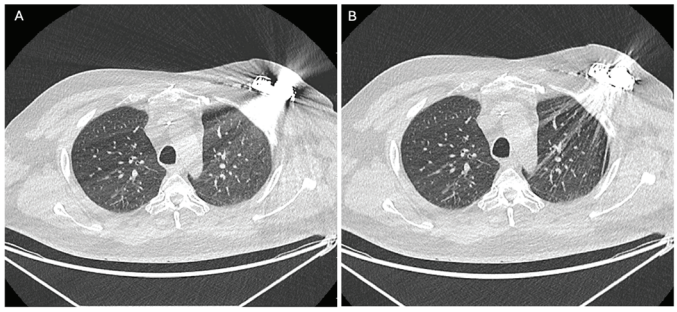

Figure 3. In the lung parenchymal window, ASIR+SMAR reduces near-field artifacts but reveals distance-dependent far-field streaks
ASIR: Adaptive statistical iterative reconstruction, SMAR: Smart metal artifact reduction

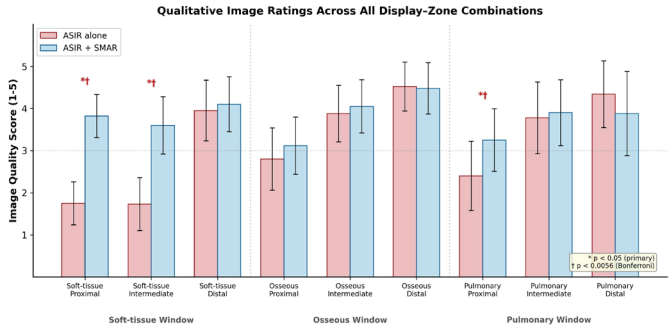

Figure 4. Aggregate qualitative scores: Reader-averaged ratings across 30 subjects demonstrating improvement with ASIR+SMAR on soft-tissue, osseous, and pulmonary displays at three distance intervals
ASIR: Adaptive statistical iterative reconstruction, SMAR: Smart metal artifact reduction

Measurement Reproducibility

Inter-observer agreement for HU-SD quantification (Reader C vs. Reader D, 10-patient subset) was excellent (ICC=0.94; 95% CI: 0.82-0.98). Intra-observer consistency (Reader C, 3-week washout, same subset) was equally high (ICC=0.96; 95% CI: 0.88–0.99).

Qualitative Image Ratings (Co-primary Endpoint 2)

Aggregate qualitative scores were significantly superior under ASIR+SMAR compared with ASIR alone (3.84±0.48 vs. 2.92±0.47; paired t-test, p<0.001; Cohen's d=1.93). Comprehensive display–zone results are presented in Table 2.

The most marked score elevations occurred on the soft-tissue display at the proximal interval (1.75±0.51 vs. 3.82±0.51; paired t-test, p<0.001; Cohen's d=1.12) and intermediate interval (1.73±0.63 vs. 3.60±0.68; paired t-test, p<0.001; Cohen's d=0.98). Both withstood Bonferroni adjustment (threshold p<0.0056).

Osseous display ratings trended upward with ASIR+SMAR at the proximal (p=0.064, Cohen's d=0.38) and intermediate (p=0.18, Cohen's d=0.34) intervals without attaining statistical significance. Conversely, pulmonary display scores were somewhat lower under ASIR+SMAR in the distal zone (4.34±0.79 vs. 3.88±1.00; Wilcoxon signed-rank, p=0.016, Cohen's d=0.52), though this difference did not survive Bonferroni correction (threshold p<0.0056).

Table 2. Qualitative image ratings by display and zone: ASIR versus ASIR+SMAR (n=30, reader-averaged)

Display-zone	ASIR (mean ± SD)	ASIR+SMAR (mean ± SD)	p-value	Cohen's d	Weighted κ (95% CI)
Global quality	2.92±0.47	3.84±0.48	<0.001*	1.93	0.72 (0.55–0.89)
Soft-tissue–Prox (<3 cm)	1.75±0.51	3.82±0.51	<0.001*†	1.12	0.70 (0.52–0.88)
Soft-tissue–Inter (3–5 cm)	1.73±0.63	3.60±0.68	<0.001*†	0.98	0.68 (0.49–0.87)
Soft-tissue–Dist (>5 cm)	3.95±0.72	4.10±0.65	0.28	0.22	0.74 (0.57–0.91)
Osseous–Prox (<3 cm)	2.80±0.74	3.12±0.68	0.064	0.38	0.66 (0.46–0.86)
Osseous–Inter (3–5 cm)	3.88±0.67	4.05±0.63	0.18	0.34	0.71 (0.53–0.89)
Osseous–Dist (>5 cm)	4.52±0.58	4.48±0.61	0.72	0.07	0.75 (0.58–0.92)
Pulmonary–Prox (<3 cm)	2.40±0.82	3.25±0.74	<0.001*†	0.86	0.69 (0.50–0.88)
Pulmonary–Inter (3–5 cm)	3.78±0.85	3.90±0.78	0.42	0.15	0.72 (0.54–0.90)
Pulmonary–Dist (>5 cm)	4.34±0.79	3.88±1.00	0.016	0.52	0.68 (0.48–0.88)

ASIR: Adaptive statistical iterative reconstruction, SMAR: Smart metal artifact reduction, SD: Standard deviation, CI: Confidence interval

Sensitivity analyses using Wilcoxon signed-rank tests across all comparisons produced outcomes concordant with the parametric results, thereby affirming the robustness of the findings irrespective of the distributional assumptions.

Algorithm-generated Artifacts

Newly emerging algorithm-related artifacts were detected in 13 of 30 individuals (43.3%; 95% CI: 25.5–62.6%). Every instance was localized to the distal pulmonary zone (>5 cm from the generator). Among these 13 cases, 8 (26.7%) exhibited low-grade streaks that still permitted diagnostic assessment (tier 2), while 5 (16.7%) exhibited high-grade degradation that precluded reliable interpretation (tier 3). The remaining 17 subjects (56.7%) were free of algorithm-related artifacts.

Reader Concordance

Weighted kappa values for qualitative scoring ranged from 0.66 to 0.75 across all display-zone pairings (Table 2), indicating substantial agreement. For aggregate image quality, weighted κ was 0.72 (95% CI: 0.55–0.89) under ASIR and 0.68 (95% CI: 0.50–0.86) under ASIR+SMAR. Structured discussion was necessary for 24 of 270 display–zone evaluations (8.9%); 20 disagreements were resolved through deliberation, while the remaining 4 (1.5%) required averaging with integer rounding.

Discussion

Key Observations

In this retrospective paired reconstruction analysis of 30 CIED carriers, the addition of SMAR to ASIR produced a marked decline in quantitative artifact intensity within the proximal zone surrounding the pulse generator, corresponding to approximately half of the baseline artifact load and indicating a large effect size. Concurrently, reader-assigned qualitative scores rose substantially, with the greatest benefit manifested in soft-tissue displays in the proximal and intermediate zones. Counterbalancing these gains, algorithm-induced streaks were observed in the distal lung parenchyma of nearly half the cohort, reaching a severity that precluded interpretation in roughly one-sixth of cases.

Practical Clinical Relevance

The enhanced proximal-zone image quality indices suggest that SMAR may improve conspicuity of peri-device tissues and adjacent vasculature, a consideration germane to the detection of complications such as device-pocket infection, hematoma formation, or thrombotic events. We stress, however, that our study quantified image quality surrogates—noise-based metrics and ordinal reader scores—rather than diagnostic accuracy parameters such as sensitivity, specificity, or downstream clinical action. Establishing whether these image quality gains yield tangible diagnostic or therapeutic benefit necessitates purpose-designed accuracy trials.

The frequency of algorithm-generated distal-zone streaks in the lung fields carries direct workflow implications, including a tangible risk of false-positive interpretations: focal artifactual densities may be mistaken for pulmonary nodules (raising spurious concern for malignancy, septic emboli, or metastatic disease); band-like streaks may simulate ground-glass opacity or consolidation; and reticular patterns may mimic early interstitial disease—each capable of triggering unnecessary follow-up imaging or invasive workup, particularly in a CIED population already burdened with cardiopulmonary comorbidities. Our data, therefore, support a dual-reconstruction review strategy whereby ASIR+SMAR datasets serve for proximal- and intermediate-zone evaluation, while unmodified ASIR images are concurrently consulted for peripheral pulmonary assessment. Any candidate parenchymal lesion seen only on the SMAR-processed series and absent on the corresponding ASIR-only reconstruction should be regarded as algorithm-induced until proven otherwise.

Technical Context

The magnitude of metallic artifacts is governed by alloy composition, physical dimensions, and hardware

geometry. Within the CIED spectrum, ICDs generally elicit more pronounced degradation than pacemakers, owing to their bulkier pulse generators and high-voltage defibrillation coils. ICDs constituted two-fifths of our cohort, potentially amplifying the observed improvements. Although formal subgroup comparison by device type was precluded by sample-size constraints, a descriptive review indicated higher baseline artifact burdens in ICD recipients than in pacemaker carriers—an observation consistent with the expected relationship between device bulk and artifact severity.

SMAR belongs to the family of projection-completion algorithms that identify and replace artifact-corrupted sinogram entries through interpolation from intact projections[16,17]. Comparable solutions from competing vendors—Siemens iMAR, Philips O-MAR, Canon SEMAR—employ distinct algorithmic approaches. Cross-platform benchmarking under standardized conditions remains an unmet need, as both the efficacy and the secondary-artifact profile of each solution may differ materially[8,18].

Contextualization with Prior Evidence

The existing literature addressing metallic artifacts arising specifically from CIEDs in thoracic CT is limited. Pennig et al.[6] investigated artifact mitigation in 34 CIED recipients using spectral-detector CT with virtual monoenergetic images and MAR post-processing, reporting effective artifact suppression around both the generator housing and endovascular leads. Their evaluation, however, centered on pectoral soft-tissue and peri-lead cardiac structures and did not extend to pulmonary parenchymal displays or to characterization of algorithm-related artifacts as a function of distance.

The present work advances this evidence base by providing display-stratified and distance-stratified assessments across soft-tissue, osseous, and pulmonary windows, delivering a more granular portrait of the spatial distribution of both artifact reduction and algorithm-induced artifact formation. The observation that SMAR confers its greatest benefit in the proximal field, while distal pulmonary artifacts remain a recurring concern, complements the findings of Pennig et al.[6] and furnishes actionable guidance for clinical radiologists.

Algorithm-Induced Artifacts: Mechanism and Precedent

Although MAR processing enhances image fidelity near metallic hardware, it may simultaneously engender secondary degradation in remote tissue, a phenomenon amply documented in the literature. Huang et al.[9] tested three MAR implementations and reported that both O-MAR and gemstone-spectral-imaging-based MAR generated new artifacts on thoracic CT. In the orthopedic domain, Shim et al.[19] demonstrated that O-MAR in shoulder arthroplasty patients can impair trabecular and cortical bone visualization, producing appearances resembling cementation or notching. These previous reports are consistent with our observation of distal lung streaks in a substantial proportion of cases.

Such artifacts are generally ascribed to overcorrection within the sinogram interpolation step, yielding dark-star patterns on axial images that correspond to zones of residual photon starvation[15,19]. Notably, not every published series has encountered newly generated artifacts; this discrepancy is likely attributable to inter-vendor algorithmic variation, differing patient populations, and the particular tissue types under scrutiny.

Study Limitations

First, the retrospective single-institution design and modest cohort size limit the strength and generalizability of the findings. In particular, the sample size may have reduced sensitivity to detect modest differences in secondary endpoints; therefore, non-significant findings in osseous-display comparisons should be interpreted with caution.

Second, deliberate exclusion of individuals with substantial pulmonary parenchymal disease—while methodologically motivated—constrains the applicability to the very population that stands to gain most from

optimized thoracic CT. Whether algorithm-generated distal-zone artifacts would obscure genuine pathology (nodules, infiltrates, interstitial abnormalities) remains unresolved and merits dedicated investigation.

Third, only one vendor's algorithm was tested under a single acquisition protocol, limiting generalizability to other MAR implementations. Fourth, systematic analysis was confined to generator-related artifacts; lead-associated degradation was not independently quantified. Fifth, the study evaluated image quality surrogates rather than diagnostic accuracy endpoints, leaving the translational impact on clinical decision-making undetermined. Any bias stemming from the exclusion of parenchymal disease could inflate the apparent benefit of MAR, because artifact assessment is inherently more straightforward against a homogeneous pulmonary background.

Subsequent investigations should prioritize: (1) multi-site comparisons of competing vendors' MAR solutions under harmonized protocols; (2) assessment of MAR utility in patients harboring defined pulmonary pathologies to gauge effects on lesion conspicuity; (3) standardized evaluation of lead-related artifacts using strategies tailored to the elongated geometry of endovascular leads—including high-keV virtual monoenergetic reconstruction from dual-energy acquisitions, photon-counting detector CT, deep learning–based MAR algorithms trained on lead morphology, lead-aware segmentation thresholds within projection-completion frameworks, and acquisition-level optimization such as tin filtration with adaptive tube current modulation; and (4) exploration of synergistic protocols coupling MAR with dual-energy CT and photon-counting detectors, which have shown promise in attenuating beam-hardening effects from metallic hardware[20,21].

Conclusion

Pairing SMAR with ASIR delivers statistically robust and clinically meaningful gains in both quantitative and qualitative image quality indices within the proximal and intermediate zones adjacent to CIED generators on thoracic CT. Soft tissues within 5 cm of the device showed the greatest benefit. Conversely, algorithm-generated artifacts in the distal lung parenchyma arise in roughly 43% of cases, with approximately 17% severe enough to impede diagnostic assessment. A combined review paradigm—leveraging ASIR+SMAR for proximal and intermediate evaluation alongside native ASIR for peripheral pulmonary appraisal—represents a pragmatic clinical workflow. These conclusions apply to individuals without significant parenchymal lung disease; corroboration in heterogeneous clinical populations and linkage to diagnostic accuracy endpoints remain essential next steps.

Ethics

Ethics Committee Approval: This retrospective analysis received institutional ethics committee approval İstanbul Yeni Yüzyıl University Clinical Research Ethics Committee (decision no: 2021/04-653, date: 06/04/2021) and conformed to the Declaration of Helsinki. The consent requirement was waived in view of the retrospective design and reliance on de-identified data.

Informed Consent: This single-institution retrospective study followed the Declaration of Helsinki and STROBE guidelines.

Data Availability

The underlying datasets may be obtained from the corresponding author upon reasonable request.

Footnotes

Authorship Contributions

Surgical and Medical Practices: Genç Ö, Concept: Genç Ö, Baş S, Tabakçı N, Design: Genç Ö, Baş S, Data Collection and/or Processing: Genç Ö, Tabakçı N, Analysis and/or Interpretation: Genç Ö, Baş S, Tabakçı N, Literature Search: Genç Ö, Writing: Genç Ö, Baş S, Tabakçı N.

Conflict of Interest: The authors declare no conflicts of interest concerning the authorship or publication of this article.

Financial Disclosure: This research received no specific grants from any funding agency in the commercial or not-for-profit sectors.

References

1. Selles M, van Osch JAC, Maas M, et al. Advances in metal artifact reduction in CT images: a review of traditional and novel metal artifact reduction techniques. Eur J Radiol. 2024;170:111276.
2. Kalisz K, Buethe J, Saboo SS, et al. Artifacts at cardiac CT: physics and solutions. Radiographics. 2016;36:2064-83.
3. Boas FE, Fleischmann D. CT artifacts: causes and reduction techniques. Imaging Med. 2012;4:229-40.
4. Fang J, Zhang D, Wilcox C, et al. Metal implants on CT: comparison of iterative reconstruction algorithms for reduction of metal artifacts with single energy and spectral CT scanning in a phantom model. Abdom Radiol. 2017;42:742-8.
5. Schwartz FR, Tailor T, Gaca JG, et al. Impact of dual energy cardiac CT for metal artefact reduction post aortic valve replacement. Eur J Radiol. 2020;129:109135.
6. Pennig L, Zopfs D, Gertz R, et al. Reduction of CT artifacts from cardiac implantable electronic devices using a combination of virtual monoenergetic images and post-processing algorithms. Eur Radiol. 2021;31:7151-61.
7. Brook OR, Gourtsoyianni S, Brook A, et al. Spectral CT with metal artifacts reduction software for improvement of tumor visibility in the vicinity of gold fiducial markers. Radiology. 2012;263:696-705.
8. Wellenberg RHH, Hakvoort ET, Slump CH, et al. Metal artifact reduction techniques in musculoskeletal CT-imaging. Eur J Radiol. 2018;107:60-9.
9. Huang JY, Kerns JR, Nute JL, et al. An evaluation of three commercially available metal artifact reduction methods for CT imaging. Phys Med Biol. 2015;60:1047-67.
10. Kidoh M, Nakaura T, Nakamura S, et al. Reduction of dental metallic artefacts in CT: value of a newly developed algorithm for metal artefact reduction (O-MAR). Clin Radiol. 2014;69:e11-e6.
11. Subhas N, Primak AN, Obuchowski NA, et al. Iterative metal artifact reduction: evaluation and optimization of technique. Skeletal Radiol. 2014;43:1729-35.
12. Chou R, Chi HY, Lin YH, et al. Comparison of quantitative measurements of four manufacturer's metal artifact reduction techniques for CT imaging. Technol Health Care. 2020;28:273-87.
13. American Association of Physicists in Medicine. Size-specific dose estimates (SSDE) in pediatric and adult body CT examinations. AAPM Report No. 204. College Park (MD): American Association of Physicists in Medicine; 2011.
14. Geyer LL, Schoepf UJ, Meinel FG, et al. State of the art: iterative CT reconstruction techniques. Radiology. 2015;276:339-57.
15. Katsura M, Sato J, Akahane M, et al. Current and novel techniques for metal artifact reduction at CT: practical guide for radiologists. Radiographics. 2018;38:450-61.
16. Bongers MN, Schabel C, Thomas C, et al. Comparison and combination of dual-energy- and iterative-based metal artefact reduction on hip prosthesis and dental implants. PLoS One. 2015;10:e0143584.
17. Lell MM, Kachelrieß M. Recent and upcoming technological developments in computed tomography. Invest Radiol. 2020;55:8-19.
18. Willemink MJ, Noël PB. The evolution of image reconstruction for CT. Eur Radiol. 2019;29:2185-95.
19. Shim E, Kang Y, Ahn JM, et al. Metal artifact reduction for orthopedic implants (O-MAR): usefulness in CT evaluation of reverse total shoulder arthroplasty. AJR Am J Roentgenol. 2017;209:860-6.
20. Rajendran K, Voss BA, Zhou W, et al. Reducing beam hardening effects and metal artifacts in spectral CT using Medipix3RX. J Instrum. 2014;9:P03015.
21. Leng S, Bruesewitz M, Tao S, et al. Photon-counting detector CT: system design and clinical applications of an emerging technology. Radiographics. 2019;39:729-43.